Solution Structure of *Mycobacterium tuberculosis* NmtR in the Apo State: Insights into Ni(II)-Mediated Allostery

Chul Won Lee,[†,‡] Dhruva K. Chakravorty,[§] Feng-Ming James Chang,[†] Hermes Reyes-Caballero,[†] Yuzhen Ye,[∥] Kenneth M. Merz, Jr.,[§] and David P. Giedroc*[†]

[†]Department of Chemistry, Indiana University, Bloomington, Indiana 47405-7102, United States
[‡]Department of Chemistry, Chonnam National University, Gwangju 500-757, Korea
[§]Department of Chemistry and Quantum Theory Project, University of Florida, Gainesville, Florida 32611-8435, United States
[∥]Program in Bioinformatics, School of Informatics and Computing, Indiana University, Bloomington, Indiana 47408, United States

S *Supporting Information*

ABSTRACT: *Mycobacterium tuberculosis* is an obligate human respiratory pathogen that encodes approximately 10 arsenic repressor (ArsR) family regulatory proteins that allow the organism to respond to a wide range of changes in its immediate microenvironment. How individual ArsR repressors have evolved to respond to selective stimuli is of intrinsic interest. The Ni(II)/Co(II)-specific repressor NmtR and related actinomycete nickel sensors harbor a conserved N-terminal α-NH$_2$-Gly2-His3-Gly4 sequence. Here, we present the solution structure of homodimeric apo-NmtR and show that the core of the molecule adopts a typical winged-helix ArsR repressor (α1-α2-α3-αR-β1-β2-α5) "open conformation" that is similar to that of the related zinc sensor *Staphylococcus aureus* CzrA, but harboring long, flexible N-terminal (residues 2–16) and C-terminal (residues 109–120) extensions. Binding of Ni(II) to the regulatory sites induces strong paramagnetic broadening of the α5 helical region and the extreme N-terminal tail to residue 10. Ratiometric pulse chase amidation mass spectrometry reveals that the rate of amidation of the α-amino group of Gly2 is strongly attenuated in the Ni(II) complex relative to the apo state and noncognate Zn(II) complex. Ni(II) binding also induces dynamic disorder on the microsecond to millisecond time scale of key DNA interacting regions that likely contributes to the negative regulation of DNA binding by Ni(II). Molecular dynamics simulations and quantum chemical calculations reveal that NmtR readily accommodates a distal Ni(II) hexacoordination model involving the α-amine and His3 of the N-terminal region and α5 residues Asp91′, His93′, His104, and His107, which collectively define a new metal sensing site configuration in ArsR family regulators.
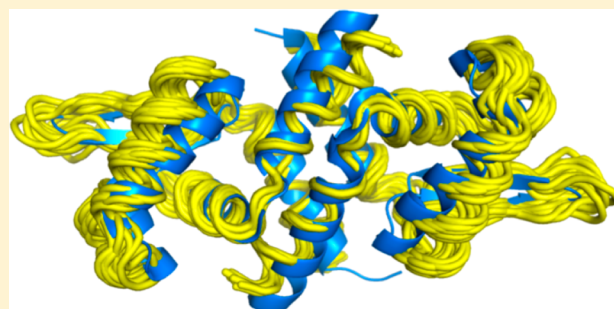
Transition metal ions, including zinc, copper, nickel, cobalt, iron, and manganese, are essential for a diversity of biological processes, the essentiality of which derives from their catalytic roles as cofactors in oxidation–reduction, electron transfer, and hydrolytic enzymes and structural roles in biomolecules.[1–3] All metal ions are toxic in excess however, and as a result, cells encode machinery to precisely control the intracellular total and bioavailable concentrations of cytoplasmic metal ions. All cells, including pathogenic organisms, have evolved the capacity to quickly respond to chronic and acute changes in the microenvironment in which the availability of both biologically essential metal ions and heavy metal pollutants varies.[4–6] The central players in this process are the metalloregulatory proteins that regulate the expression of genes encoding metal transporters and trafficking proteins, which collectively manage metal homeostasis and resistance.[6,7]

Mycobacterium tuberculosis (*Mtb*) is the causative pathogen of human tuberculosis. *Mtb* encodes a remarkable diversity of known and putative metal ion transporters, including multiple putative P-type ATPases, ABC transporters, and cation diffusion facilitator (CDF) transporters.[8] A large panel of metalloregulatory proteins in *Mtb* regulate transcription of those transporters. For example, *Mtb* CsoR represses transcription of the *cso* (Cu-sensitive operon) that encodes CsoR itself, a Cu(I)-effluxing P-type ATPase CtpV, and a gene of unknown function.[9] *Mtb* also encodes approximately 10 arsenic repressor (ArsR) family proteins that regulate the expression of genes encoding proteins responsible for metal ion detoxification, sequestration, efflux, and perhaps other processes.[10–13]

Several members of the ArsR family have been extensively studied.[5,12] Among them, *Staphylococcus aureus* Zn(II) sensor CzrA is the most well characterized family repressor with regard to our structural, mechanistic, and thermodynamic understanding of allosteric negative regulation of DNA operator

binding.[14−18] *S. aureus* CzrA represses the transcription of the cation diffusion facilitator (CDF) CzrB in the absence of metal stress.[19,20] The quaternary structure of CzrA adopts a typical winged-helix homodimeric fold[21,22] denoted an "α5" ArsR family sensor.[23] CzrA binds Zn(II) with negative homotropic cooperativity[15,17] at two regulatory tetrahedral sites positioned across the pair of C-terminal α5 helices. A previous site-specific mutagenesis study of CzrA revealed that two metal ligands were necessary to maintain the native coordination geometry and Zn(II)-mediated regulation, while two other ligands were required only for maintaining high metal binding affinity with no or small effects on regulation, in what is termed a "division of labor" organization.[15] Altogether, it has been suggested that the metal coordination geometry is a fundamental determinant of metal selectivity for metalloregulators.[7,14,24] The recent nuclear magnetic resonance (NMR) structure of CzrA in the DNA-bound state suggested that metal binding drives a "closed-to-open" conformational change to reduce the affinity of DNA binding and induced long-range disorder in the allosteric metal sites.[16,18]

There are two Ni(II)-specific ArsR repressors encoded by *Mtb*.[11,25] These are NmtR and KmtR, which repress the transcription of *ctpJ* and *cdf*, encoding a P-type ATPase metal transporter and a putative cation diffusion facilitator (CDF) transporter, respectively, at low Ni(II) concentrations. At high Ni(II) concentrations, NmtR and KmtR bind Ni(II) and dissociate from their DNA operators, allowing transcription of *ctpJ* and *cdf*, to export Ni(II) and Co(II), respectively, from the cytoplasm.[8,11] A previous in vivo study proposed that NmtR binds Ni(II) in an octahedral coordination geometry with four metal ligands in the α5 helix, D91, H93, H104, and H107, and two C-terminal residues, H109 and H116.[25] We recently proposed an alternative Ni(II) coordination model involving the N-terminal Gly2-His3-Gly4 motif in NmtR (in place of H109 and H116) that specifically drives Ni(II) binding and allosteric negative regulation of DNA binding on the basis of in vitro metal binding and DNA binding assays of a collection of conservative glutamine substitution mutants.[26]

Here we present the solution NMR structure of homo-dimeric NmtR in the apo state. The overall structure reveals a typical core winged-helix fold of the ArsR family, but with distinct long flexible N- and C-terminal tails. The binding of paramagnetic Ni(II) induces strong line broadening of the regulatory sites composed of α5 helices as well as the N-terminal tail to residue 10. In contrast, residues in the C-terminal tail beyond position 110 (residues 111−120) are unaffected by Ni(II) binding; as such, these findings rule out Ni(II) coordination by His116. Ratiometric pulse chase amidation mass spectrometry[27] reveals that the α-amino group of Gly2 is strongly protected from amidination in the Ni(II)-bound form, with the noncognate, tetrahedral Zn(II) complex[14] providing little significant protection relative to the apo state. These and previous findings taken collectively are consistent with a regulatory octahedral Ni(II) complex formed by the α-amine and His3 from the N-terminus and α5 residues Asp91', His93', His104', and His107'. This chelate structure is supported by a range of molecular dynamics (MD) simulations[18] of the noncognate Zn(II) and cognate Ni(II) complexes.

■ EXPERIMENTAL PROCEDURES

Protein Purification. Recombinant NmtR was expressed and purified as described previously.[26] For the NMR experiments, ^{15}N-labeled or [13]C- and ^{15}N-labeled NmtR was expressed in *Escherichia coli* BL21(DE3) cells in M9 minimal medium and purified essentially as described previously.[16,26] MALDI-TOF mass spectrometry of purified apo-NmtR used in this work reveals a molecular mass of 12699.7 Da (value of 12704.3 Da expected for residues 2−120, with the N-terminal Met processed).[26]

NMR Spectroscopy. For NMR experiments, NmtR was prepared in 10 mM Hepes (pH 7.0) and 100 mM NaCl in a 10% [2]H$_2$O/90% H$_2$O mixture or 100% [2]H$_2$O at protomer protein concentrations ranging from 0.35 to 0.50 mM. All NMR experiments were performed on a Varian DDR 600 or 800 MHz spectrometer fitted with cryogenic probe systems at 310 K in the METACyt Biomolecular NMR Laboratory. NMR spectra were referenced to external DSS. NMR data processing and analysis were performed using NMRPipe[28] and NMRView.[29] Backbone resonance assignments were obtained using the standard triple-resonance NMR data set as described previously.[26] Assignments of side chain resonances were made using three-dimensional (3D) HCCH-COSY,[30] H(CCO)NH-TOCSY,[31,32] and C(CO)NH-TOCSY[32] experiments. Distance restraints were derived from 3D ^{15}N-edited NOESY-HSQC (τ_m = 100 ms) and ^{13}C-edited NOESY-HSQC (τ_m = 80 ms) spectra. Backbone amide residual dipolar couplings, $^1D_{NH}$, were obtained from the difference in the scalar coupling (^1J) measured in stretched polyacrylamide gels (4%) using two-dimensional IPAP-HSQC spectroscopy.[33]

Structure Calculations. NOE cross-peak assignments and initial NOE constraints were obtained with CYANA 2.1[34] and CANDID.[35] All NOE constraints were manually confirmed during CYANA calculations. Hydrogen bonds for the helical regions of NmtR were added to facilitate the automated assignment of additional NOE restraints by CANDID. Chemical shift-based restraints from TALOS+[36] were included only for regions of secondary structure.

The initial 100 symmetric homodimer structures were calculated by a simulated annealing protocol with Xplor-NIH[37] and were further refined with the addition of noncrystallographic symmetry (NCS) and RDC restraints. A total of 54 intersubunit NOE restraints were cross-validated during the structure calculation procedure by randomly removing one-third of these constraints and recalculating the global precision of the structures.[16] Iterative refinement and editing of the distance restraints based on the NOESY spectra to remove incorrect and ambiguous assignments reduced the number of restraints. The final 19 structures with the lowest energy were chosen for analysis and were deposited in the Protein Data Bank (entry 2LKP).

Simulations of NmtRs. Molecular dynamics simulations of the apo, Zn(II)-bound, and Ni(II)-bound allosteric forms of NmtR were performed using the AMBER 11 suite of programs[38,39] utilizing the ff99SBildn[40] force field. The protonation states for charged amino acids not involved in metal binding were obtained from the H++ protonation state server.[41] In simulations of Zn(II)·NmtR and Ni(II)·NmtR, the metal binding residues in the α5 helix (Asp91, His93, His104' and His107') were represented in protonation states adopted from the Zn(II)-bound crystal structure of CzrA.[22] A protonation state model similar to that employed in our previous simulations of apo-CzrA featuring a positively charged His104 and a negatively charged Asp91 was found to be the most likely candidate for apo-NmtR.[18]

A common solvation and equilibration scheme was implemented to prepare the allosteric forms of NmtR for production MD simulations. The protein was immersed in a periodically replicated truncated octahedral box containing explicit SPC/E water molecules[42,43] that provided an 8 Å water shell around it. In these simulations, a range of 11578−26933 water molecules was used to solvate the protein. The solvated protein was next net-neutralized using explicit Na+ or Cl− counterions.[44] A single Cl− ion was required to neutralize the apo allosteric form of the protein, while two additional Cl− ions were required to neutralize the metal ion-bound forms of the protein. The systems were prepared for production simulations using a well-defined equilibration protocol. First, a series of restrained minimizations was performed in which constituent parts of the system were gradually relaxed over multiple stages to prevent artifacts and steric clashes. In the first phase of minimization, the water molecules and counterions were minimized while the protein was kept restrained. Employing a multistage approach, increasingly larger parts of the protein were gradually relaxed. In the subsequent stages of minimization, protein hydrogen atom positions were optimized followed by a minimization including side chain groups. In the next stage of energy minimization, only the backbone $C\alpha$ atoms were kept restrained, and in the final step, the entire protein structure was minimized along with the solvent molecules and counterions. The phases of minimization were performed for 10000, 10000, 20000, 40000, and 40000 steps, unless convergence was achieved earlier. The minimized system was then slowly heated to 300 K for a canonical ensemble (*NVT*) over 200 ps, while weak restraints on all protein heavy atoms were maintained. Finally, all restraints were removed, and the system was further equilibrated for 1 ns at 300 K for an isobaric and isothermal ensemble (*NPT*). MD trajectories were propagated from this well-equilibrated structure at 300 K for an *NPT* ensemble. The temperature of the simulated system was maintained using Langevin dynamics with a collision frequency of 1 ps^{-1}, and the SHAKE algorithm was employed to constrain heavy atom bonds to hydrogen atoms.[42,45,46] Long-range electrostatics were calculated using the particle mesh Ewald method.[47] A time step of 2 fs was employed, and snapshots from the trajectories were collected for analysis after every 1000 steps.

Modeling the Zn(II) Binding Site of NmtR. Starting from a solvated and well-equilibrated structure of apo-NmtR, we used constrained MD and energy minimization methods to bring the possible metal binding residues to within a reasonable distance for Zn(II) binding. A Zn(II) ion was placed at each metal binding site using the Maestro GUI.[48] Both metal binding regions [D91, H93, H104, H107, and Zn(II))] were treated using density functional theory (DFT)-based QM/MM methods[49] (M06-L/LACVP* for QM and OPLS-2005 force field for MM residues)[50−53] as implemented in the Qsite QM/MM program.[50]

To further validate the calculated binding site of Zn(II)-bound NmtR and to capture the effect of Zn(II) binding on the entire protein structure, we performed 1 ns of QM/MM MD[54] simulations on solvated and well-equilibrated Zn(II)·NmtR and Zn$_2$·NmtR structures at the SCC-DFTB level of theory[55,56] using the AMBER suite of programs. A detailed description of these QM/MM and QM/MM MD calculations and their successful implementation has been provided elsewhere.[18,57,58] The bond distances and relative orientations of coordinating residues in this α5 site of NmtR are similar to those observed in CzrA.[18]

Modeling of the Ni(II) Binding Site. We performed model system calculations at the DFT level of theory to validate the proposed Ni(II) coordination complex in NmtR. These calculations included the Ni(II) ion coordinated to Gly2, His3, and a reduced representation of Asp91, His93, His104, and His107. We used the Gaussian09 electronic structure program[59] to perform these calculations with the M06-L functional[51] paired with the valence double-ζ polarized 6-31G* basis set for C and H atoms, the 6-31+G* basis set for O and N atoms, and the LANL2TZ effective core potentials for Ni(II).[60−63] The calculated Ni(II) bond lengths from these calculations were similar to those obtained from XAS experiments.[14] We then performed steered MD (SMD) calculations in an effort to determine whether the N-terminal amino acids (Gly2 and His3) could access the distal and proximal binding models of Ni(II) coordination (Figure S2 of the Supporting Information). In these calculations, Gly2 and His3 were "reeled in" from distances of tens of angstroms into the proximal and distal Ni(II) binding sites over hundreds of picoseconds. The tetracoordinated metal ion was represented using our previously developed "bonded model" parameters for a DHHH binding motif using MTK++.[64,65] Preliminary simulations performed using a generalized Born implicit solvent model[66,67] indicated that introducing Gly2 and His3 at the distal Ni(II) coordination sites caused large changes in the structure of the protein. Analogous simulations in which Gly2 and His3 were introduced into the proximal Ni(II) coordination sphere failed to elicit a similar conformational change, suggesting that the distal binding mode was the correct representation. To create a model construct for Ni(II)-bound NmtR and validate the distal binding mode, multiple SMD simulations in which Gly2 and His3 were introduced into the distal metal binding site in explicit solvent were performed. These simulations were initiated from explicitly solvated and well-equilibrated structures of tetracoordinated Ni$_2$·NmtR and were performed over tens of nanoseconds.

Ratiometric Pulse Chase Amidination Mass Spectrometry (rPAm-MS). These mass-coded experiments were conducted essentially as described previously;[27] a pulse of *S*-methyl thioacetimidate (SMTA) was added for time *t*, followed by a chase with an excess of *S*-methyl thiopropionimidate (SMTP) (Δ = 14 amu), quenched, and digested with trypsin, and the N-terminal heptapeptide (^{2}GHGVEGR^8) was quantified by high-resolution matrix-assisted laser desorption ionization time-of-flight (MALDI-TOF) mass spectrometry. The expected molecular mass of acetamidinated peptide 2−8 is 752.4 Da, while that of propionamidinated peptide 2−8 is 766.4 Da. NmtR monomer (containing 20 μM total amine) was reacted in either the apo, Zn(II)-bound (2.5 mol of monomer/equiv of Zn), or Ni(II)-bound (1.5 mol of monomer/equiv of Ni) state and mixed with a 100-fold (apo-NmtR and Zn(II)·NmtR) or 500-fold (Ni(II)·NmtR) monomer molar excess of SMTA, followed by a 2000-fold (apo and Zn-bound states) or 10000-fold (Ni state) monomer molar excess of SMTP. Quantitation of the intensities (I) of the acetimidated (A) and propionimidated (P) peptides as a function of time *t* was conducted as previously described[27] with the mole fraction propionimidated (Θ^P) calculated from the equation $\Theta^P = I_P/(I_A + I_P)$. Each data set was fit to the single-exponential decay $\Theta^P = A_o e^{-kt}$ to obtain *k* and divided by [SMTA] in the pulse to obtain the second-order rate constant (M_{SMTA}^{-1} min^{-1}).

■ RESULTS AND DISCUSSION

Solution Structure of Apo-NmtR. Uniformly [15]N- and ^{13}C-labeled apo-NmtR that conforms to the sequence in Figure S1 of the Supporting Information (residues 2–120, with the N-terminal Met processed)[26] was subjected to detailed multidimensional NMR analysis using standard methods to obtain nearly complete backbone assignments (Cα, Hα, C′, N, and H[N]) and ≈90% of the assignments of the side chain protons. The structure was calculated on the basis of 509 intraprotomer and 54 interprotomer [1]H–[1]H NOE restraints and 49 [1]D_{NH} RDCs per protomer (Table 1). The final ensemble of 19

Table 1. NMR Restraints and Structural Statistics for the Apo-NmtR Homodimer[a]

no. of NMR restraints	
total NOE distance restraints	563
intrasubunit restraints	509
intersubunit restraints	54
hydrogen bond restraints	96
total dihedral angle restraints	142
RDC restraints	46
structural statistics (19 structures)	
violations	
no. of distance restraints >0.5 Å	0
no. of dihedral angle restraints >5°	0
rmsd from experiments	
distances (Å)	0.065 ± 0.006
dihedral angles (deg)	0.464 ± 0.013
rmsd from idealized geometry	
bonds (Å)	0.004 ± 0.000
angles (deg)	0.643 ± 0.136
impropers (deg)	0.390 ± 0.020
Ramachandran analysis (%) (all residues)	
most favored region	81.8
additionally allowed region	13.1
generously allowed region	4.3
disallowed region	0.7
average pairwise rmsd (Å) (residues 17–108)[b]	
backbone heavy atoms	1.47 ± 0.42
all heavy atoms	2.17 ± 0.39

[a]Resonance assignments and other NMR data for apo-NmtR have been deposited in the BioMagResBank as entry 18003, with structure bundle apo-NmtR deposited in the Protein Data Bank as entry 2LKP. [b]Coordinate precision was calculated by comparing individual structures in the bundle with the coordinates of the average structure. Only residues 17–108 for each subunit were used in this analysis.

structures shows excellent statistics and structural convergence with a final pairwise heavy atom root-mean-square deviation (rmsd) of 1.47 ± 0.42 Å (Table 1).

A ribbon representation of a global superposition of the 19 models is shown in Figure 1, compared to the average structure, from the DNA binding interface (Figure 1A) and the allosteric sites (Figure 1B). The core of apo-NmtR adopts the typical ArsR repressor (α1-α2-α3-α4-β1-β2-α5) fold encompassing residues 17–108 as previously observed in *Mtb* CmtR,[68] *S. aureus* CadC,[69] and *Xylella fastidiosa* BigR[13] and in the zinc sensors *S. aureus* CzrA[16,22] and *Synechococcus* SmtB[22,70] but in this case is flanked by long unstructured, highly mobile N-terminal (residues 2–16) and C-terminal (residues 109–120) "tails".[26] These tails emerge on opposite sides of the

molecule with the N-terminal tail of one protomer closest to the C-terminal tail of the other protomer (Figure 1). Helix α4 is the DNA recognition helix, also denoted αR. The β-wing tip is structurally less well-defined than the core of the molecule, as was previously found in solution for Zn(II)-bound CzrA.[16] There is no evidence from these data that NmtR harbors an additional N-terminal α-helix like that present in the α3N Cd/Pb sensor CadC.[23,69]

S. aureus CzrA is strongly related to *Mtb* NmtR (≈30% identical and ≈60% similar), and detailed comparative studies of this pair of sensors have long served as a model system with which to investigate the evolution of metal selectivity in ArsR family repressors.[5,6,14,71] In fact, CzrA can be considered NmtR without the tails, and indeed, both sensors harbor a standard "α5-type" metal binding Asp1-x-His2-x_{10}-His3-x_2-His/Glu4 motif (where x is any amino acid) (Figure S1 of the Supporting Information).[12,72] In CzrA, this sequence is found in helix α5, and the two symmetry-related, interprotomer zinc-sensing sites are defined by tetrahedral coordination to Asp1-His2-His3′-His4′ and Asp1′-His2′-His3-His4 sites (Figure S2 of the Supporting Information). CzrA is selective for Zn(II) and shows no response to Ni(II); in contrast, NmtR is selective for Ni(II) and Co(II) and shows an attenuated response (in vitro) or no response (in vivo) to Zn(II).[6,14,25] Although our structure establishes that the core folds of NmtR and CzrA are similar, a global superposition of the core apo-NmtR structure bundle with the average structure (Figure 2A) reveals detectable differences compared to that of the bundle superimposed on the crystallographic structure of apo-CzrA (Figure 2B). These differences extend beyond the uncertainty of the coordinates of the structure bundle and derive at least partly from distinct protomer packing (≈1.6 Å Cα rmsd) (Figure 2B). In any case, apo-NmtR, like apo-CzrA, clearly adopts an open dimer conformation, in which the interprotomer Ser61 Cα–Ser61′ Cα distance is quite large (≈48 Å), a distance comparable with the largest analogous (Ser54–Ser54′ Cα) distance observed in molecular dynamics simulations of allosterically inhibited Zn(II)·CzrA.[18] This form of apo-NmtR is clearly not preorganized to bind DNA without a significant change to a more "closed" conformation, perhaps like that previously observed for apo-CzrA.[16]

Paramagnetic Broadening Induced by Ni(II) Directly Implicates the N-Terminal Tail and the C-Terminal α5 Helix As Providing Ligand Donor Atoms to the Ni(II). Addition of Ni(II) to apo-NmtR induces significant changes in the ^{15}N TROSY spectrum, including a number of shifts superimposed on a significant reduction in the number of crosspeaks (Figure S3 of the Supporting Information). Ni(II) is expected to broaden resonances within ≈10 Å of the paramagnetic, high-spin Ni(II),[73,74] consistent with a six-coordinate, distorted octahedral geometry determined previously.[14] These spectral perturbations are shown in a bar chart (Figure 3A) and schematically on a ribbon representation of the solution structural model from three different views (Figure 4). What is clearly seen is that Ni(II) binding extensively broadens resonances at the extreme N-terminus (from residue 4 to 10; residues 2 and 3 are unassigned in the apo state[26]) as well as residues at both the N-terminal and C-terminal regions of the α5 helix (residues 91–93 are exchange broadened in apo-NmtR[26]), and extending to only L110, after which point there is little observable broadening.

These spectral features are consistent with the conclusions reached earlier on the basis of thermodynamic measurements of
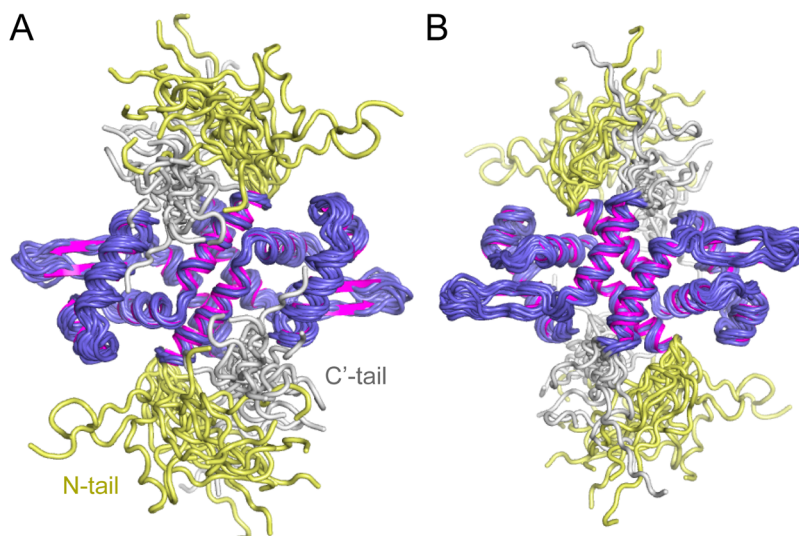
Figure 1. Ribbon representation of the solution structure of apo-NmtR. The nineteen lowest-energy structures (Protein Data Bank entry 2LKP) are colored yellow (residues 2−16), indigo (residues 17−107), and gray (residues 108−120) superimposed on the average structure (residues 16−107) colored magenta. (A) View from the $\alpha 1 - \alpha$R DNA binding interface; (B) View from the allosteric $\alpha 5$ helices.
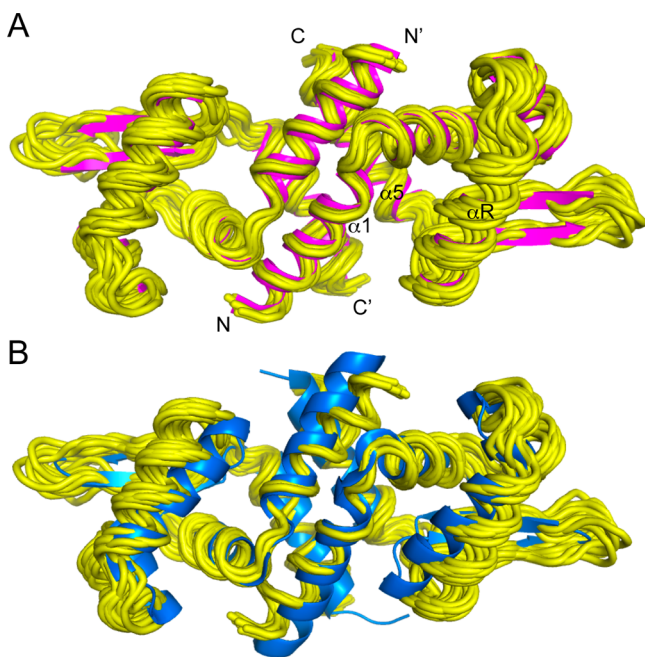

Figure 2. Ribbon representation of the folded core of apo-NmtR (residues 17−107). The bundle of 19 structures (yellow) is globally superimposed on the average structure (magenta) (A) and on the crystallographic structure of *S. aureus* CzrA (colored marine blue, Protein Data Bank entry 1R1U). The values of the subunit pairwise Cα rmsd (using residues 9−101 or 9−102 in CzrA and residues 17−107 for NmtR) are 1.62 and 1.69 Å, respectively, while the dimer pairwise Cα rmsd is 2.53 Å. αR, DNA recognition helix $\alpha 4$.

the K_{Ni} and allosteric coupling free energy, ΔG_c^{Ni}, and suggest that the Ni(II) binds to four residues analogous to the tetrahedral zinc complex of CzrA (D91, H93, H104, and H107) and the two residues derived from the extreme N-terminus, the α-amino group and the side chain of His3.[26] Although these studies do not distinguish between proximal (P) and distal (D) Ni(II) binding site models (see Figure 4B and Figure S2 of the Supporting Information), it is interesting to note that there is complete broadening of residues 4−10, and L15 just
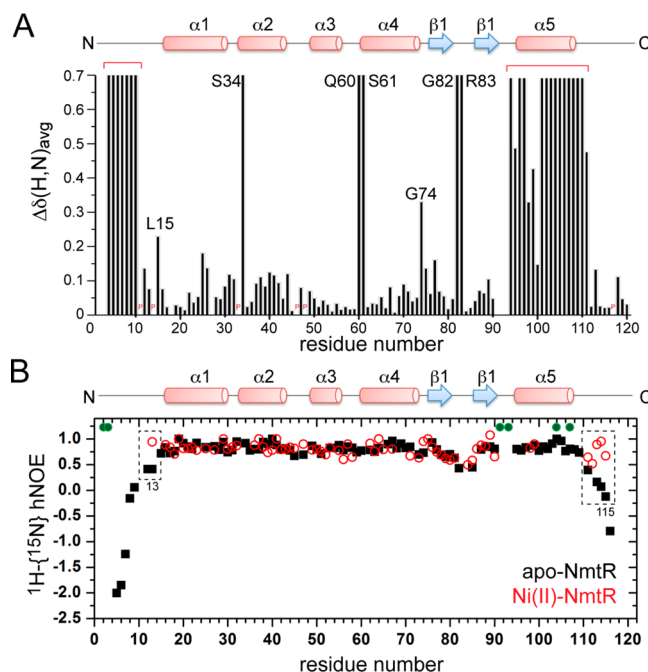

Figure 3. Perturbations of ^{15}N−^{1}H HSQC spectra of binding of Ni(II) to apo-NmtR. (A) Chemical shift changes as a function of residue number. Resonances broadened beyond detection in the paramagnetic Ni(II) complex are arbitrarily assigned a $\Delta \delta(H,N)_{avg}$ value of 0.7, and those close to the Ni(II) are clustered by the red bracket. Perturbations for other residues for which a resonance cross-peak is observed are calculated with the equation $\Delta \delta(H,N)_{avg} = [(\Delta \delta_{HN})^2 + (\Delta \delta_N / 5)^2]^{1/2}$. Resonances of interest are highlighted, and a secondary structure schematic is shown at the top of the figure. P, Pro residue. Residues 91−93 are conformationally exchange broadened in the apo state,[26] and thus, no data are shown for these residues. (B) Plot of ^{1}H−$\{^{15}$N$\}$ heteronuclear NOE vs residue number for apo-NmtR[26] (●) and Ni(II)·NmtR (red circles). Regions of significant difference between the two states are boxed, and proposed Ni(II) ligands are denoted with the green circles.

N-terminal to helix $\alpha 1$ is strongly shifted upon Ni(II) binding. Given the relatively short-range (≈ 10 Å) paramagnetic sphere
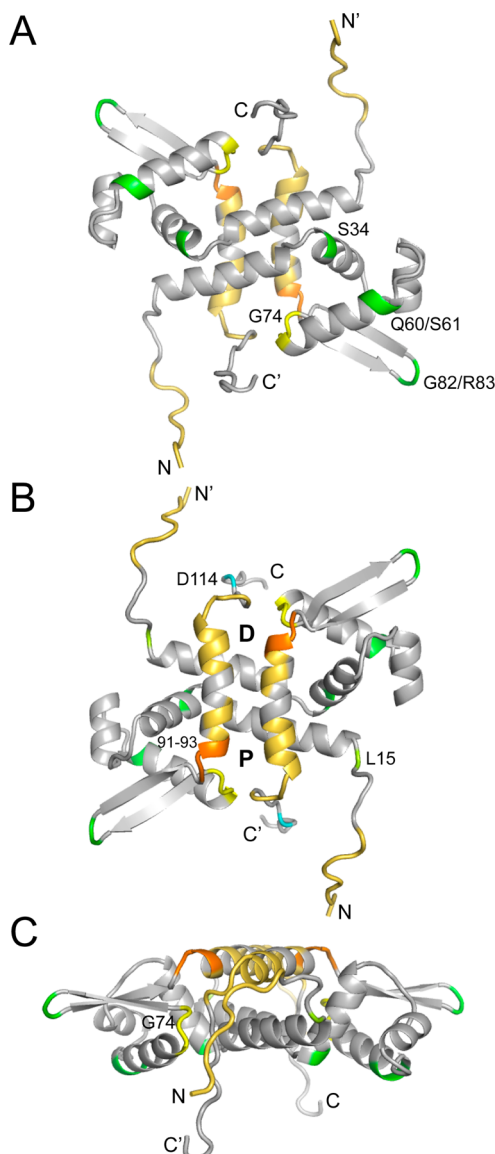
Figure 4. Schematic representation of the spectral perturbations of binding of Ni(II) to apo-NmtR painted on the ribbon representation of the average structure of apo-NmtR from three different views: (A) bottom, DNA binding interface, (B) "top" or allosteric site view, and (C) side view. All residues for which backbone amide correlations are paramagnetically broadened or shifted are colored gold, while residues 91−93 (conformationally broadened in apo-NmtR) are highlighted in orange. Green denotes backbone amides conformationally broadened in Ni(II)·NmtR far from the metal site (see Figure 3A), with L15 (B) and G74 (C) highlighted because of significant perturbations in chemical shift. In panel B, D114 (cyan) defines the penultimate C-terminal residue that is ordered upon Ni(II) binding (see also Figure S5 of the Supporting Information). D and P define the proximal and distal α5 metal sites, respectively, relative to the N-terminus labeled N at the bottom right. See also Figure S2 of the Supporting Information.

of influence of the bound Ni(II), only in the distal binding mode would a substantial region of the N-terminal tail pass close enough to one Ni(II) ion or the other to result in paramagnetic broadening (see Figure 4B). Thus, these data favor a model in which the Ni(II) forms an octahedral complex via coordination by G2, H3, D91′, H93′, H104, and H107 and its symmetry-related pair (Figure S2 of the Supporting Information) (see below).

Because of the unfavorable spectral characteristics of the Ni(II) complex, we were unable to obtain a structural model of the Ni(II) complex. Inspection of the ^{1}H−{^{15}N} heteronuclear NOE reveals that Ni(II) binding stabilizes both the N-terminal (to residue 13) and C-terminal (to residue 115) tail regions compared to apo-NmtR, such that these regions now tumble on the picosecond to nanosecond time scale with the rest of the protein (Figure 3B). The structural origin of this conformational ordering is unknown, but for the vast majority of residues, Ni(II)-induced conformational changes are quaternary structural in nature, given the high degree of correspondence of ^{13}Cα chemical shifts (where they are observable) in the apo and Ni(II)-bound states (Figure S4 of the Supporting Information).

We also acquired NMR data for the noncognate Zn(II)-bound NmtR, and Figure S3 of the Supporting Information shows an overlay of ^{15}N TROSY spectra of the apo, Ni(II)-bound, and Zn(II)-bound complexes. Inspection of these spectra suggests that the conformational change induced by Zn(II) is distinct from that of Ni(II), but we could do little else with the Zn(II)·NmtR sample given the poor solubility of this metalated derivative. X-ray absorption spectroscopy reveals a tetrahedral Zn(II) complex, and QM/MM calculations reveal that a first coordination complex formed by the α5 residues only (Asp91, His93, His104′, and His107′) that is fully consistent with the data can be modeled (Figure 5A). Thus,
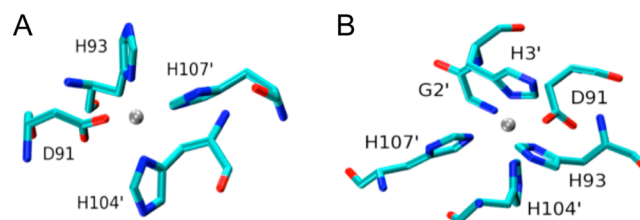

Figure 5. Results of quantum mechanical and molecular mechanical molecular dynamics (QM/MM MD) calculations of the noncognate Zn(II) complex (A) and steered molecular dynamics simulations of the cognate Ni(II) complex (B) of NmtR.[14] Panel B is rotated ≈90° along the vertical relative to panel A. Metal−ligand distances varied from calculation to calculation and were found to range from 1.95 to 2.20 Å in our models. For the model shown, the Ni(II)−ligand distances are 1.96 Å for Gly2 α-amino N, 2.09 Å for His3 Nδ1, 1.96 Å for Asp91 Oδ1, 2.14 Å for His104 Nδ1, and 2.11 Å for His107 Nε2. Residue identities are indicated with prime nomenclature indicative of the opposite protomer. See Experimental Procedures for full details.

these data and previous studies[26] argue that Zn(II) is a weaker allosteric regulator than Ni(II) because it does not recruit the extreme N-terminus into the first metal coordination shell and thus is incapable of fully switching NmtR to an allosterically inhibited conformation.[71]

In striking contrast, an identical series of calculations reveals that it is indeed possible to recruit two ligands from the N-terminus to create a pseudooctahedral complex with good stereochemistry around the Ni(II) ion (Figure 5B; see also Figure S5 of the Supporting Information). In this complex, the Nδ1 atoms of His3 and His104 are the axial ligands to the octahedrally coordinated Ni(II) ion, with the α-NH$_2$ group, Asp91′, His93′ (Nδ1), and His107 (Nε2) lying roughly in a plane. Multiple SMD calculations suggest that in this coordination model, the N-terminus reaches over the top of the α5 helices to coordinate to the distal α5 metal site (Figure 6). In models derived from these calculations, the Nε2 face of
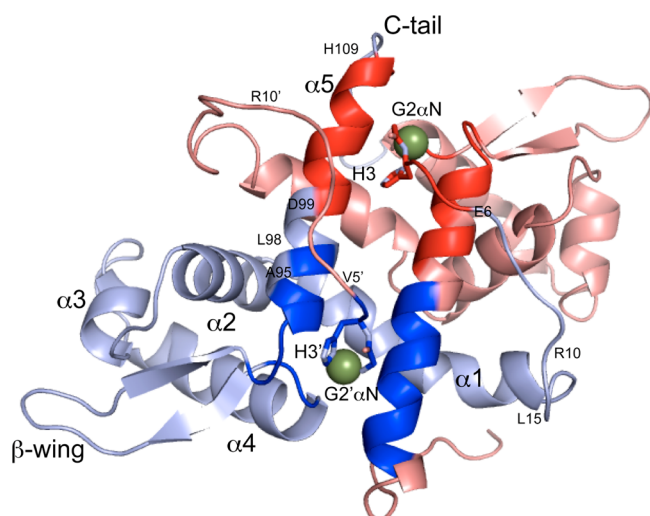
Figure 6. Ribbon diagram of a MD-derived model of the Ni(II)-bound NmtR with each N-terminus coordinating to the distal Ni(II) site, such the N-terminal tails cross the C-terminal $\alpha5$ helices. Each protomer is colored light blue and salmon, and Ni(II) ions are colored green. The Gly2 α-NH$_2$ group and His3 Nδ1 are shown coordinated to the Ni(II); other coordinating side chains (D91, H93, H104, and H107) are not shown for the sake of clarity. A zone of 10 Å around each Ni(II) ion is colored blue and red; this is the region in which one expects to see complete paramagnetic broadening on amide cross-peaks (compare to Figure 3A). The agreement between theory and experiment is excellent, with the exception of residues 6−10 (see the text for details).

His104 points toward the backbone carbonyl groups of Leu73′ and Gly74′ and in some instances specifically forms a hydrogen bond with the backbone carbonyl group of Gly74. Such a hydrogen bonding interaction could explain the perturbations in the ^{15}N−^{1}H HSQC spectra observed at Gly74 in response to Ni(II) binding (Figure 3A) and suggests that a CzrA-like hydrogen bonding pathway[18] may play a role in the mechanism of allosteric regulation. The structure shown (Figure 6) is in excellent agreement with the paramagnetic broadening observed in the NMR spectra of Ni(II)·NmtR in detail (Figure 3A), except for residues 6−10 in the N-terminal region. Although these resonances are experimentally broadened beyond detection (Figure 3A), in this model these residues are just outside of the zone of paramagnetic influence of the Ni(II) ions ($\leq$13 Å) (Figure 6). It is important to recognize that the precise path that each N-terminal tail takes is not well-defined by these simulations. However, these SMD models suggest that a number of favorable electrostatic interactions between charged residues in the N-terminal region and $\alpha5$ helices of NmtR may stabilize the distal binding model. On the other hand, if these residues do indeed lie outside of the Ni(II) broadening zone, then conformational exchange might be contributing to dynamic disorder in this region. Additional studies are required to distinguish between these two possibilities.

Ratiometric Pulsed Amidation Mass Spectrometry. To obtain additional evidence of the participation of the N-terminal α-amino group in Ni(II) coordination, we took advantage of the fact that NmtR contains no lysine residues, with the only primary amine being the N-terminal α-NH$_2$ group (see Figure S1 of the Supporting Information). We reasoned that the reactivity of the α-amine with respect to an amine-modifying reagent would be greatly attenuated in the

Ni(II)-bound state versus the apo state or the Zn(II)-bound state, which adopts a tetrahedral coordination geometry (Figure 5A).[14,26,71] A ratiometric pulsed amidation mass spectrometry method was used to obtain second-order rate constants for amidation of the α-amino group in these allosteric states.[27] Here, NmtR is reacted with a pulse of S-methyl thioacetimidate (SMTA) for time t, followed by a chase with an excess of S-methyl thiopropionimidate (SMTP) (Δ = 14 amu), with the reaction quenched and protein subsequently digested with trypsin. Tryptic peptides are then subjected to high-resolution MALDI-TOF mass spectrometry and peak areas of the amidinated (SMTA) and propionimidated (SMTP) N-terminal heptapeptide (^{2}GHGVEGR^8) quantified by integration. The raw mass spectrometry of this region of the mass spectrum is shown in Figure 7, with the data fit to a single exponential to extract the pseudo-first-order rate constant for amidation (k) (Figure 8) and second-order rate constants listed in Table 2. These data reveal that the α-amino group is highly reactive in the apo state ($\approx$94 M^{-1} min^{-1}) and is at most 2-fold protected when bound to noncognate metal ion Zn(II) ($\approx$50 M^{-1} min^{-1}). In strong contrast, Ni(II) affords 100-fold protection relative to apo-NmtR ($\approx$1 M^{-1} min^{-1}). These data taken collectively strongly support the Ni(II) coordination model shown in Figure 5B in which the α-amino group of Gly2 forms a direct coordination bond to the Ni(II) ion via a multidentate interaction with other donor atoms in the N-terminal region, e.g., His3,[26] as found in other proteins involved in Ni(II) sensing and trafficking.[75−78]

Dynamical Changes in NmtR upon Ni(II) Binding and Implications for DNA Operator Binding. Although the paramagnetic zone of influence broadens beyond detection those residues within $\approx$10 Å of the bound Ni(II) ions,[74] there are other changes in the ^{15}N−^{1}H HSQC spectrum of Ni(II)-bound NmtR that are likely reporting on changes in conformational dynamics that are important for Ni(II)-mediated negative regulation of DNA binding (Figure 3A). In particular, inspection of the DNA binding interfacial region reveals several ^{15}N−^{1}H correlations that are significantly exchange broadened beyond detection upon Ni(II) binding, including those corresponding to S34 near the N-terminus of $\alpha2$, Q60 and S61 at the N-terminus of the $\alpha4$ recognition helix, and G82 and R83 at the tip of the β-wing (Figure 4 and Figure S6 of the Supporting Information). These residues are conserved in at least eight of nine of the candidate NmtRs (see Figure S1 of the Supporting Information) and correspond to N27, Q53, S54, G75, and Q76 in the related zinc sensor *S. aureus* CzrA.[14] Q53E and S54A substitutions in CzrA show 4800- and 10^5-fold reductions in DNA binding affinity, respectively,[16] and inspection of the molecular dynamics-based model of the apo-CzrA−DNA operator complex[18] reveals that all five residues define key contact regions across the entire protein−DNA interface (Figure S7 of the Supporting Information). Although the structure of the apo-NmtR−DNA complex is not yet available, these residues likely define the interfacial region of the NmtR−DNA complex as well, given the very high level of conservation of the residues in the DNA recognition $\alpha4$ helices and the near identity of the DNA operators to which CzrA and NmtR bind (NmtO, 5′-**TGAA**CATATG**ATCA**; CzrO, 5′-**TGA-ACAAATATTCA**).[16] If so, these data suggest that Ni(II)-induced dynamic disorder on the microsecond to millisecond time scale of key DNA interacting regions contributes to the negative regulation of DNA binding.
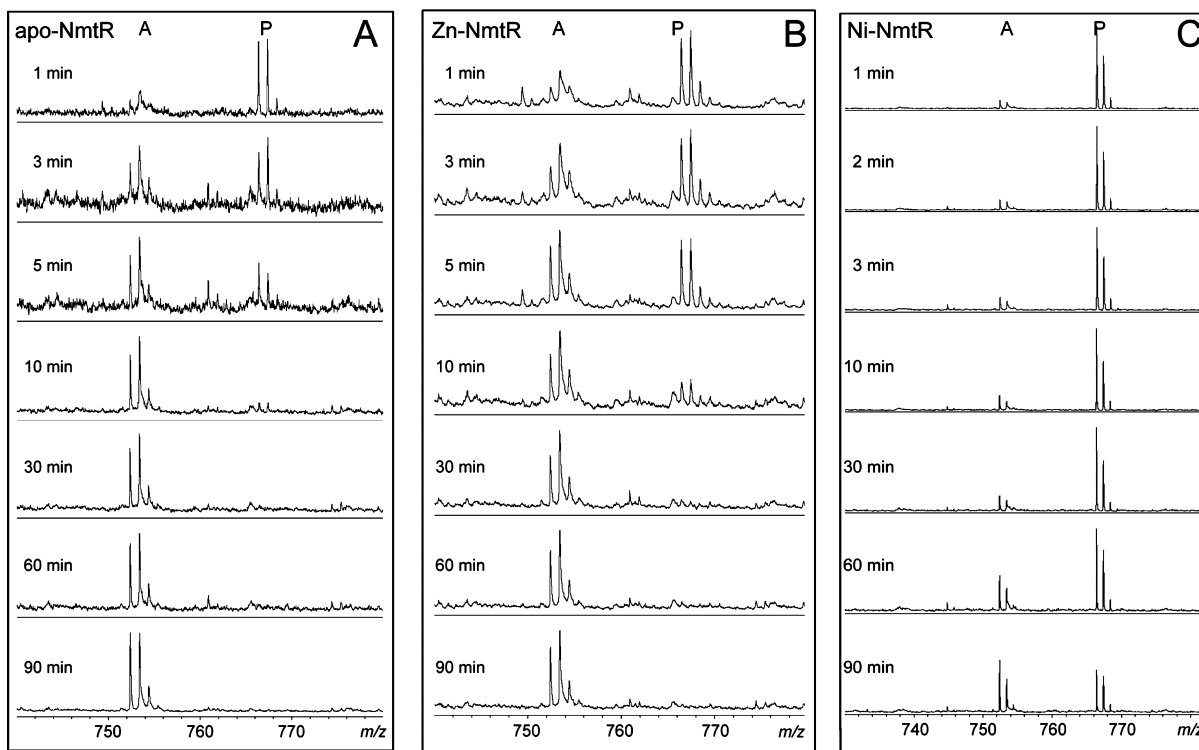
Figure 7. Series of MALDI-TOF spectra of tryptic peptide 2–8 as a function of pulse amidination time (*t*) in apo-NmtR (A), Zn(II)·NmtR (B), and Ni(II)·NmtR (C). The isotope distributions of two different modified peptides are labeled A (singly acetamidinated) (752.34 Da observed value, 752.40 Da expected value) and P (singly propionamidinated) (766.34 Da observed value, 766.40 Da expected value) with observed *m/z* values.
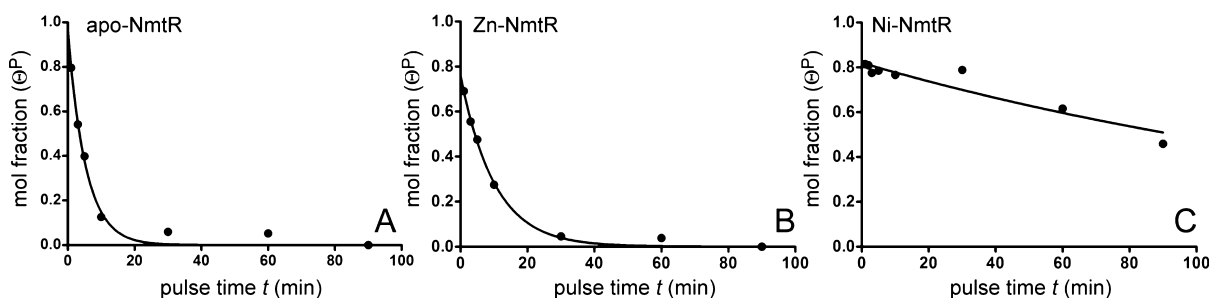

Figure 8. Mole fractions of the propionamidinated α-amino group, Θ^P, plotted as a function of pulse amidination time (*t*) in apo-NmtR (A), Zn(II)·NmtR (B), and Ni(II)·NmtR (C). Pseudo-first-order rate constants were determined by fitting the data with the single-exponential decay $\Theta = Ae^{-kt}$ with parameters listed in Table 2.

Table 2. Second-Order Amidination Rate Constants Obtained for the α-Amino Groups of Various NmtRs[a]

NmtR	second-order rate constant ($M_{SMTA}^{-1}\ min^{-1}$)	amplitude (A_o)
apo	93.5 ± 9.8	0.96 ± 0.05
Zn(II)-bound	49.2 ± 10.1	0.76 ± 0.02
Ni(II)-bound	0.96 ± 0.43	0.82 ± 0.02

[a]Derived from the data shown in Figures 7 and 8 by fitting Θ^P vs pulse time to a single-exponential function with no offset.

The amide group cross-peak corresponding to G74 in the turn between the α4 and β1 strands is also significantly broadened and shifted upon Ni(II) binding (Figure 4C). G74 corresponds to His67 in CzrA, the backbone carbonyl group of which accepts an intersubunit hydrogen bond from the nonliganding side chain of H97′ (H104′) to stabilize the allosterically inhibited low-DNA

binding affinity conformation.[18,22] This suggests the possibility that this key interprotomer H104′–G74 linkage plays an important role in allosteric coupling by Ni(II) in NmtR, as well, which explains in part why Zn(II) drives some negative regulation of DNA binding in NmtR even without coordination to the extreme N-terminus.[26]

■ CONCLUSIONS

In this work, we present the solution structure of the Ni- and Co-specific ArsR family regulator NmtR from *Mtb* and propose a Ni(II) coordination model that is consistent with previous thermodynamic experiments,[26] X-ray absorption spectroscopy,[14] chemical modification, and Ni(II)-induced paramagnetic broadening measurements. Molecular dynamics simulations and quantum chemical calculations reveal such a coordination model can be readily accommodated by the structure of NmtR. It is unknown as yet precisely how distal Ni(II) site

coordination by the extreme N-terminus drives a structural change in the dimer that mediates allosteric negative regulation of *nmt* DNA operator-promoter binding, except to say that loss of N-terminal coordination changes the coordination number and the rank order of allosteric effectors from Ni(II) > Zn(II) to Zn(II) > Ni(II).[26] Efforts are underway to obtain a high-resolution structural model of the Ni(II)·NmtR complex.

■ ASSOCIATED CONTENT

Ⓢ Supporting Information

Supplementary Figures S1—S7. This material is available free of charge via the Internet at http://pubs.acs.org.

■ AUTHOR INFORMATION

Corresponding Author

*Department of Chemistry, Indiana University, 212 S. Hawthorne Dr., Bloomington, IN 47405-7102. E-mail: giedroc@indiana.edu. Telephone: (812) 856-3178. Fax: (812) 856-5710.

Notes

The authors declare no competing financial interest.

■ ACKNOWLEDGMENTS

■ REFERENCES

(1) Berg, J. M., and Godwin, H. A. (1997) Lessons from zinc-binding peptides. *Annu. Rev. Biophys. Biomol. Struct. 26*, 357—371.

(2) Seneque, O., Bonnet, E., Joumas, F. L., and Latour, J. M. (2009) Cooperative metal binding and helical folding in model peptides of treble-clef zinc fingers. *Chemistry 15*, 4798—4810.

(3) Auld, D. S. (2001) Zinc coordination sphere in biochemical zinc sites. *BioMetals 14*, 271—313.

(4) Giedroc, D. P., and Arunkumar, A. I. (2007) Metal sensor proteins: Nature's metalloregulated allosteric switches. *Dalton Trans. 29*, 3107—3120.

(5) Ma, Z., Jacobsen, F. E., and Giedroc, D. P. (2009) Coordination chemistry of bacterial metal transport and sensing. *Chem. Rev. 109*, 4644—4681.

(6) Reyes-Caballero, H., Campanello, G. C., and Giedroc, D. P. (2011) Metalloregulatory proteins: Metal selectivity and allosteric switching. *Biophys. Chem. 156*, 103—114.

(7) Chen, P. R., and He, C. (2008) Selective recognition of metal ions by metalloregulatory proteins. *Curr. Opin. Chem. Biol. 12*, 214—221.

(8) Agranoff, D., and Krishna, S. (2004) Metal ion transport and regulation in *Mycobacterium tuberculosis*. *Front. Biosci. 9*, 2996—3006.

(9) Liu, T., Ramesh, A., Ma, Z., Ward, S. K., Zhang, L., George, G. N., Talaat, A. M., Sacchettini, J. C., and Giedroc, D. P. (2007) CsoR is a novel *Mycobacterium tuberculosis* copper-sensing transcriptional regulator. *Nat. Chem. Biol. 3*, 60—68.

(10) Busenlehner, L. S., Pennella, M. A., and Giedroc, D. P. (2003) The SmtB/ArsR family of metalloregulatory transcriptional repressors: Structural insights into prokaryotic metal resistance. *FEMS Microbiol. Rev. 27*, 131—143.

(11) Campbell, D. R., Chapman, K. E., Waldron, K. J., Tottey, S., Kendall, S., Cavallaro, G., Andreini, C., Hinds, J., Stoker, N. G.,

Robinson, N. J., and Cavet, J. S. (2007) Mycobacterial cells have dual nickel-cobalt sensors: Sequence relationships and metal sites of metal-responsive repressors are not congruent. *J. Biol. Chem. 282*, 32298—32310.

(12) Osman, D., and Cavet, J. S. (2010) Bacterial metal-sensing proteins exemplified by ArsR-SmtB family repressors. *Nat. Prod. Rep. 27*, 668—680.

(13) Guimaraes, B. G., Barbosa, R. L., Soprano, A. S., Campos, B. M., de Souza, T. A., Tonoli, C. C., Leme, A. F., Murakami, M. T., and Benedetti, C. E. (2011) Plant pathogenic bacteria utilize biofilm growth-associated repressor (BigR), a novel winged-helix redox switch, to control hydrogen sulfide detoxification under hypoxia. *J. Biol. Chem. 286*, 26148—26157.

(14) Pennella, M. A., Shokes, J. E., Cosper, N. J., Scott, R. A., and Giedroc, D. P. (2003) Structural elements of metal selectivity in metal sensor proteins. *Proc. Natl. Acad. Sci. U.S.A. 100*, 3713—3718.

(15) Pennella, M. A., Arunkumar, A. I., and Giedroc, D. P. (2006) Individual metal ligands play distinct functional roles in the zinc sensor *Staphylococcus aureus* CzrA. *J. Mol. Biol. 356*, 1124—1136.

(16) Arunkumar, A. I., Campanello, G. C., and Giedroc, D. P. (2009) Solution structure of a paradigm ArsR family zinc sensor in the DNA-bound state. *Proc. Natl. Acad. Sci. U.S.A. 106*, 18177—18182.

(17) Grossoehme, N. E., and Giedroc, D. P. (2009) Energetics of allosteric negative coupling in the zinc sensor *S. aureus* CzrA. *J. Am. Chem. Soc. 131*, 17860—17870.

(18) Chakravorty, D. K., Wang, B., Lee, C. W., Giedroc, D. P., and Merz, K. M. (2012) Simulations of allosteric motions in the zinc sensor CzrA. *J. Am. Chem. Soc. 134*, 3367—3376.

(19) Kuroda, M., Hayashi, H., and Ohta, T. (1999) Chromosome-determined zinc-responsible operon *czr* in *Staphylococcus aureus* strain 912. *Microbiol. Immunol. 43*, 115—125.

(20) Singh, V. K., Xiong, A., Usgaard, T. R., Chakrabarti, S., Deora, R., Misra, T. K., and Jayaswal, R. K. (1999) ZntR is an autoregulatory protein and negatively regulates the chromosomal zinc resistance operon *znt* of *Staphylococcus aureus*. *Mol. Microbiol. 33*, 200—207.

(21) Gajiwala, K. S., and Burley, S. K. (2000) Winged helix proteins. *Curr. Opin. Struct. Biol. 10*, 110—116.

(22) Eicken, C., Pennella, M. A., Chen, X., Koshlap, K. M., VanZile, M. L., Sacchettini, J. C., and Giedroc, D. P. (2003) A metal-ligand-mediated intersubunit allosteric switch in related SmtB/ArsR zinc sensor proteins. *J. Mol. Biol. 333*, 683—695.

(23) Busenlehner, L. S., Weng, T. C., Penner-Hahn, J. E., and Giedroc, D. P. (2002) Elucidation of primary (α3N) and vestigial (α5) heavy metal-binding sites in *Staphylococcus aureus* pI258 CadC: Evolutionary implications for metal ion selectivity of ArsR/SmtB metal sensor proteins. *J. Mol. Biol. 319*, 685—701.

(24) Waldron, K. J., Rutherford, J. C., Ford, D., and Robinson, N. J. (2009) Metalloproteins and metal sensing. *Nature 460*, 823—830.

(25) Cavet, J. S., Meng, W., Pennella, M. A., Appelhoff, R. J., Giedroc, D. P., and Robinson, N. J. (2002) A nickel-cobalt-sensing ArsR-SmtB family repressor. Contributions of cytosol and effector binding sites to metal selectivity. *J. Biol. Chem. 277*, 38441—38448.

(26) Reyes-Caballero, H., Lee, C. W., and Giedroc, D. P. (2011) *Mycobacterium tuberculosis* NmtR harbors a nickel sensing site with parallels to *Escherichia coli* RcnR. *Biochemistry 50*, 7941—7952.

(27) Chang, F. M., Lauber, M. A., Running, W. E., Reilly, J. P., and Giedroc, D. P. (2011) Ratiometric pulse-chase amidination mass spectrometry as a probe of biomolecular complex formation. *Anal. Chem. 83*, 9092—9099.

(28) Delaglio, F., Grzesiek, S., Vuister, G. W., Zhu, G., Pfeifer, J., and Bax, A. (1995) NMRPipe: A multidimensional spectral processing system based on UNIX pipes. *J. Biomol. NMR 6*, 277—293.

(29) Johnson, B. A., and Blevins, R. A. (1994) NMR View: A computer program for the visualization and analysis of NMR data. *J. Biomol. NMR 5*, 603—614.

(30) Bax, A., Clore, G. M., and Gronenborn, A. M. (1990) ^{1}H-^{1}H correlation via isotropic mixing of ^{13}C magnetization, a new three-dimensional approach for assigning ^{1}H and ^{13}C spectra of ^{13}C-enriched proteins. *J. Magn. Reson. 88*, 425—431.

(31) Montelione, G. T., Lyons, B. A., Emerson, S. D., and Tashiro, M. (1992) An efficient triple resonance experiment using carbon-13 isotropic mixing for determining sequence-specific resonance assignments of isotopically-enriched proteins. *J. Am. Chem. Soc. 114*, 10974−10975.

(32) Grzesiek, S., Anglister, J., and Bax, A. (1993) Correlation of backbone amide and aliphatic side-chain resonances in $^{13}C/^{15}N$-enriched proteins by isotropic mixing of ^{13}C magnetization. *J. Magn. Reson. 101*, 114−119.

(33) Ding, K., and Gronenborn, A. M. (2003) Sensitivity-enhanced 2D IPAP, TROSY-anti-TROSY, and E.COSY experiments: Alternatives for measuring dipolar ^{15}N-^1HN couplings. *J. Magn. Reson. 163*, 208−214.

(34) Guntert, P. (2004) Automated NMR structure calculation with CYANA. *Methods Mol. Biol. 278*, 353−378.

(35) Herrmann, T., Guntert, P., and Wuthrich, K. (2002) Protein NMR structure determination with automated NOE assignment using the new software CANDID and the torsion angle dynamics algorithm DYANA. *J. Mol. Biol. 319*, 209−227.

(36) Shen, Y., Delaglio, F., Cornilescu, G., and Bax, A. (2009) TALOS+: A hybrid method for predicting protein backbone torsion angles from NMR chemical shifts. *J. Biomol. NMR 44*, 213−223.

(37) Schwieters, C. D., Kuszewski, J. J., Tjandra, N., and Clore, G. M. (2003) The Xplor-NIH NMR molecular structure determination package. *J. Magn. Reson. 160*, 65−73.

(38) Case, D. A., Darden, T. A., Cheatham, T. E., III, Simmerling, C. L., Wang, J., Duke, R. E., Luo, R., Walker, R. C., Zhang, W., Merz, K. M., Roberts, B., Wang, B., Hayik, S., Roitberg, A., Seabra, G., Kolossvai, I., Wong, K. F., Paesani, F., Vanicek, J., Liu, J., Wu, X., Brozell, S. R., Steinbrecher, T., Gohlke, H., Cai, Q., Ye, X., Wang, J., Hsieh, M.-J., Cui, G., Roe, D. R., Mathews, D. H., Seetin, M. G., Sagui, C., Babin, V., Luchko, T., Gusarov, S., Kovalenko, A., and Kollman, P. A. (2010) *AMBER 11*, University of California, San Francisco.

(39) Case, D. A., Cheatham, T. E. III, Darden, T., Gohlke, H., Luo, R., Merz, K. M. Jr., Onufriev, A., Simmerling, C., Wang, B., and Woods, R. J. (2005) The Amber biomolecular simulation programs. *J. Comput. Chem. 26*, 1668−1688.

(40) Lindorff-Larsen, K., Piana, S., Palmo, K., Maragakis, P., Klepeis, J. L., Dror, R. O., and Shaw, D. E. (2010) Improved side-chain torsion potentials for the Amber ff99SB protein force field. *Proteins: Struct., Funct., Bioinf. 78*, 1950−1958.

(41) Gordon, J. C., Myers, J. B., Folta, T., Shoja, V., Heath, L. S., and Onufriev, A. (2005) H++: A server for estimating pK_as and adding missing hydrogens to macromolecules. *Nucleic Acids Res. 33*, W368−W371.

(42) Allen, M. P., and Tildesley, D. J. (1987) *Computer Simulations of Liquids*, Clarendon Press, Oxford, U.K.

(43) van der Spoel, D., van Maaren, P. J., and Berendsen, H. J. C. (1998) A systematic study of water models for molecular simulation: Derivation of water models optimized for use with a reaction field. *J. Chem. Phys. 108*, 10220−10230.

(44) Joung, I. S., and Cheatham, T. E. III (2008) Determination of alkali and halide monovalent ion parameters for use in explicitly solvated biomolecular simulations. *J. Phys. Chem. B 112*, 9020−9041.

(45) Adelman, S. A., and Doll, J. D. (1976) Generalized Langevin equation approach for atom-solid-surface scattering: General formulation for classical scattering off harmonic solids. *J. Chem. Phys. 64*, 2375−2388.

(46) Doll, J. D., and Dion, D. R. (1976) Generalized Langevin equation approach for atom-solid-surface scattering: Numerical techniques for Gaussian generalized Langevin dynamics. *J. Chem. Phys. 65*, 3762−3766.

(47) York, D. M., Darden, T. A., and Pedersen, L. G. (1993) The effect of long-range electrostatic interactions in simulations of macromolecular crystals: A comparison of the Ewald and truncated list methods. *J. Chem. Phys. 99*, 8345−8348.

(48) Tools, M.-D. I. (2011) *Maestro-Desmond Interoperability Tools*, version 3.0, Schrödinger, New York.

(49) Senn, H. M., and Thiel, W. (2009) QM/MM Methods for Biomolecular Systems. *Angew. Chem. Int. Ed. 48*, 1198−1229.

(50) *Qsite*, version 5.7 (2011) Schrödinger, New York.

(51) Zhao, Y., and Truhlar, D. G. (2008) The M06 suite of density functionals for main group thermochemistry, thermochemical kinetics, noncovalent interactions, excited states, and transition elements: Two new functionals and systematic testing of four M06-class functionals and 12 other functionals. *Theor. Chem. Acc. 120*, 215−241.

(52) Cramer, C. J., and Truhlar, D. G. (2009) Density functional theory for transition metals and transition metal chemistry. *Phys. Chem. Chem. Phys. 11*, 10757−10816.

(53) Jorgensen, W. L., and Tirado-Rives, J. (2005) Chemical Theory and Computation Special Feature: Potential energy functions for atomic-level simulations of water and organic and biomolecular systems. *Proc. Natl. Acad. Sci. U.S.A. 102*, 6665−6670.

(54) Hartsough, D. S., and Merz, K. M. (1995) Dynamic force field models: Molecular dynamics simulations of human carbonic anhydrase II using a quantum mechanical/molecular mechanical coupled potential. *J. Phys. Chem. 99*, 11266−11275.

(55) Seabra, G. D., Walker, R. C., Elstner, M., Case, D. A., and Roitberg, A. E. (2007) Implementation of the SCC-DFTB method for hybrid QM/MM simulations within the Amber molecular dynamics package. *J. Phys. Chem. A 111*, 5655−5664.

(56) Gaus, M., Cui, Q. A., and Elstner, M. (2011) DFTB3: Extension of the self-consistent-charge density-functional tight-binding method (SCC-DFTB). *J. Chem. Theory Comput. 7*, 931−948.

(57) Chakravorty, D. K., Wang, B., Ucisik, M. N., and Merz, K. M. (2011) Insight into the cation-π interaction at the metal binding site of the copper metallochaperone CusF. *J. Am. Chem. Soc. 133*, 19330−19333.

(58) Yang, Y., Wang, B., Ucisik, M. N., Cui, G., Fierke, C. A., and Merz, K. M. (2012) Insights into the mechanistic dichotomy of the protein farnesyltransferase peptide substrates CVIM and CVLS. *J. Am. Chem. Soc. 134*, 820−823.

(59) Frisch, M. J., Trucks, G. W., Schlegel, H. B., Scuseria, G. E., Robb, M. A., Cheeseman, J. R., Montgomery, J. A., Jr., Vreven, T., Kudin, K. N., Burant, J. C., Millam, J. M., Iyengar, S. S., Tomasi, J., Barone, V., Mennucci, B., Cossi, M., Scalmani, G., Rega, N., Petersson, G. A., Nakatsuji, H., Hada, M., Ehara, M., Toyota, K., Fukuda, R., Hasegawa, J., Ishida, M., Nakajima, T., Honda, Y., Kitao, O., Nakai, H., Klene, M., Li, X., Knox, J. E., Hratchian, H. P., Cross, J. B., Bakken, V., Adamo, C., Jaramillo, J., Gomperts, R., Stratmann, R. E., Yazyev, O., Austin, A. J., Cammi, R., Pomelli, C., Ochterski, J. W., Ayala, P. Y., Morokuma, K., Voth, G. A., Salvador, P., Dannenberg, J. J., Zakrzewski, V. G., Dapprich, S., Daniels, A. D., Strain, M. C., Farkas, O., Malick, D. K., Rabuck, A. D., Raghavachari, K., Foresman, J. B., Ortiz, J. V., Cui, Q., Baboul, A. G., Clifford, S., Cioslowski, J., Stefanov, B. B., Liu, G., Liashenko, A., Piskorz, P., Komaromi, I., Martin, R. L., Fox, D. J., Keith, T., Al-Laham, M. A., Peng, C. Y., Nanayakkara, A., Challacombe, M., Gill, P. M. W., Johnson, B., Chen, W., Wong, M. W., Gonzalez, C., and Pople, J. (2009) *Gaussian 09*, version A.01, Gaussian, Inc., Wallingford, CT.

(60) Petersson, G. A., Bennett, A., Tensfeldt, T. G., Allaham, M. A., Shirley, W. A., and Mantzaris, J. (1988) A Complete Basis Set Model Chemistry. 1. The Total Energies of Closed-Shell Atoms and Hydrides of the 1st-Row Elements. *J. Chem. Phys. 89*, 2193−2218.

(61) Petersson, G. A., and Allaham, M. A. (1991) A Complete Basis Set Model Chemistry. 2. Open-Shell Systems and the Total Energies of the 1st-Row Atoms. *J. Chem. Phys. 94*, 6081−6090.

(62) Wadt, W. R., and Hay, P. J. (1985) Ab initio effective core potentials for molecular calculations: Potentials for main group elements Na to Bi. *J. Chem. Phys. 82*, 284−298.

(63) Roy, L. E., Hay, P. J., and Martin, R. L. (2008) Revised basis sets for the LANL effective core potentials. *J. Chem. Theory Comput. 4*, 1029−1031.

(64) Peters, M. B., Yang, Y., Wang, B., Fusti-Molnar, L., Weaver, M. N., and Merz, K. M. (2010) Structural survey of zinc-containing proteins and development of the zinc AMBER force field (ZAFF). *J. Chem. Theory Comput. 6*, 2935−2947.

(65) Yang, Y., Chakravorty, D. K., and Merz, K. M. Jr. (2010) Finding a needle in the haystack: Computational modeling of Mg^{2+} binding in the active site of protein farnesyltransferase. *Biochemistry 49*, 9658−9666.

(66) Bashford, D., and Case, D. A. (2000) Generalized Born models of macromolecular solvation effects. *Annu. Rev. Phys. Chem. 51*, 129−152.

(67) Sitkoff, D., Sharp, K. A., and Honig, B. (1994) Accurate calculation of hydration free-energies using macroscopic solvent models. *J. Phys. Chem. 98*, 1978−1988.

(68) Banci, L., Bertini, I., Cantini, F., Ciofi-Baffoni, S., Cavet, J. S., Dennison, C., Graham, A. I., Harvie, D. R., and Robinson, N. J. (2007) NMR structural analysis of cadmium sensing by winged helix repressor CmtR. *J. Biol. Chem. 282*, 30181−30188.

(69) Ye, J., Kandegedara, A., Martin, P., and Rosen, B. P. (2005) Crystal structure of the *Staphylococcus aureus* pI258 CadC Cd(II)/Pb(II)/Zn(II)-responsive repressor. *J. Bacteriol. 187*, 4214−4221.

(70) Cook, W. J., Kar, S. R., Taylor, K. B., and Hall, L. M. (1998) Crystal structure of the cyanobacterial metallothionein repressor SmtB: A model for metalloregulatory proteins. *J. Mol. Biol. 275*, 337−346.

(71) Guerra, A. J., and Giedroc, D. P. (2011) Metal site occupancy and allosteric switching in bacterial metal sensor proteins. *Arch. Biochem. Biophys. 519*, 210−222.

(72) VanZile, M. L., Chen, X., and Giedroc, D. P. (2002) Structural characterization of distinct α3N and α5 metal sites in the cyanobacterial zinc sensor SmtB. *Biochemistry 41*, 9765−9775.

(73) Pochapsky, T. C., Pochapsky, S. S., Ju, T., Hoefler, C., and Liang, J. (2006) A refined model for the structure of acireductone dioxygenase from *Klebsiella* ATCC 8724 incorporating residual dipolar couplings. *J. Biomol. NMR 34*, 117−127.

(74) Pochapsky, S. S., Sunshine, J. C., and Pochapsky, T. C. (2008) Completing the circuit: Direct-observe $^{13}C,^{15}N$ double-quantum spectroscopy permits sequential resonance assignments near a paramagnetic center in acireductone dioxygenase. *J. Am. Chem. Soc. 130*, 2156−2157.

(75) Iwig, J. S., Leitch, S., Herbst, R. W., Maroney, M. J., and Chivers, P. T. (2008) Ni(II) and Co(II) sensing by *Escherichia coli* RcnR. *J. Am. Chem. Soc. 130*, 7592−7606.

(76) Barondeau, D. P., Kassmann, C. J., Bruns, C. K., Tainer, J. A., and Getzoff, E. D. (2004) Nickel superoxide dismutase structure and mechanism. *Biochemistry 43*, 8038−8047.

(77) Sankararamakrishnan, R., Verma, S., and Kumar, S. (2005) ATCUN-like metal-binding motifs in proteins: Identification and characterization by crystal structure and sequence analysis. *Proteins 58*, 211−221.

(78) Chung, K. C., Cao, L., Dias, A. V., Pickering, I. J., George, G. N., and Zamble, D. B. (2008) A high-affinity metal-binding peptide from *Escherichia coli* HypB. *J. Am. Chem. Soc. 130*, 14056−14057.